Barotropic instability in the West Spitsbergen Current

S. H. Teigen,[1] F. Nilsen,[1,2] and B. Gjevik[3]

[1]   Barotropic instability in the shoreward branch of the West Spitsbergen Current is investigated on the basis of data from an array of current meter moorings along 78.83°N, across the upper continental slope and shelf break west of Svalbard. The slowly varying background current profile is modeled as an along-slope, asymmetric jet anchored to the shelf break. Numerical linear stability analyses are performed on the idealized current profile and topography, revealing the characteristic period, wavelength, and growth rate of unstable vorticity waves. Detailed analysis of the ambient current profile in 2007–2008 shows that unstable conditions are present during ~40% of the 10 month measurement record, depending on the localization, width, and amplitude of the current jet. The resulting vorticity waves are localized at the shelf break and are able to exchange water masses across the oceanic Arctic front. Typical wavelengths and periods are 20–40 km and 40–70 h, respectively. Wavelet, coherence, and complex demodulation analyses of the current meter data confirm that transient signals of similar periodicity as predicted by the stability analysis exist in the data record, prominently during the winter and spring months. Estimates of the heat loss contribution from isopycnal diffusion reach 1.4 TW during the time intervals when unstable vorticity waves are active at the shelf break, implying that the dynamics of the West Spitsbergen Current play a significant role in the cooling process of the Atlantic water on the way to the Arctic Ocean. This cooling corresponds to an along-shelf cooling rate of $-0.08°C$ per 100 km.

1.   Introduction

[2]   The West Spitsbergen Current (WSC) is the main contributor of oceanic heat and salt to the Arctic Ocean [*Aagaard and Greisman*, 1975]. The habitual description of the WSC identifies it as the continuation of the primarily barotropic slope branch of the Norwegian Atlantic Current. More recently, *Walczowski and Piechura* [2007] have shown evidence that the baroclinic offshore branch of the Norwegian Atlantic Current, guided by the Mohn Ridge and Knipovich Ridge into the Fram Strait, converges with the slope branch at about 78°N (Figure 1). The Fram Strait fracture zones and diverging isobaths cause the WSC to split again into several branches [*Quadfasel et al.*, 1987]. Westward turning branches follow the Hovgaard, Molloy, and Spitsbergen fracture zones across the Fram Strait and flow south with the East Greenland Current [*Quadfasel et al.*, 1987; *Bourke et al.*, 1988; *Manley*, 1995; *Fahrbach et al.*, 2003]. North of 79°N, the slope current bifurcates into the Yermak branch and the Svalbard branch [*Aagaard et al.*, 1987]. The Yermak branch continues northward, following the western rim of the Yermak Pla-

teau, where it mixes with ambient waters by tidal mixing [*Gascard et al.*, 1995]. The Svalbard branch crosses over the 600 m deep Yermak Plateau and is responsible for the bulk of Atlantic input to the Arctic Ocean [*Saloranta and Haugan*, 2001]. The exact volume fraction of the Yermak branch that recirculates directly into the Fram Strait and the fraction that rejoins the Svalbard branch after a loop around the Yermak Plateau are still uncertain [*Manley*, 1995]. *Schauer et al.* [2008] reported that the temperature of the northward flowing Atlantic water (AW) in the Fram Strait increased by 0.50°C from 1998 to 2000 and another 0.50°C between 2003 and 2006. *Dmitrenko et al.* [2008] showed that the warming signal has propagated into the Eurasian Basin. Upstream heat loss and mixing with surrounding water masses influence the depth level at which the Atlantic water input to the Arctic Ocean occurs. As it flows north along the continental slope west of Svalbard, the subsurface core of the current (the layer between 100 and 500 m depth) over the upper slope is cooled by $\sim-0.20°C$ per 100 km during summer and $\sim-0.31°C$ per 100 km during winter [*Saloranta and Haugan*, 2004]. The corresponding heat flux from the 100–500 m layer is -1050 W m^{-2}, which is 2.5–3 times larger than the estimated heat flux from the 0–100 m surface layer. This is too large to be solely attributed to direct vertical heat loss to the atmosphere. The WSC displays a complex, multipath flow structure with characteristic features like meandering and frequent mesoscale eddying [*Gascard et al.*, 1995]. The

---

[1]Department of Arctic Geophysics, University Centre in Svalbard, Longyearbyen, Norway.
[2]Geophysical Institute, University of Bergen, Bergen, Norway.
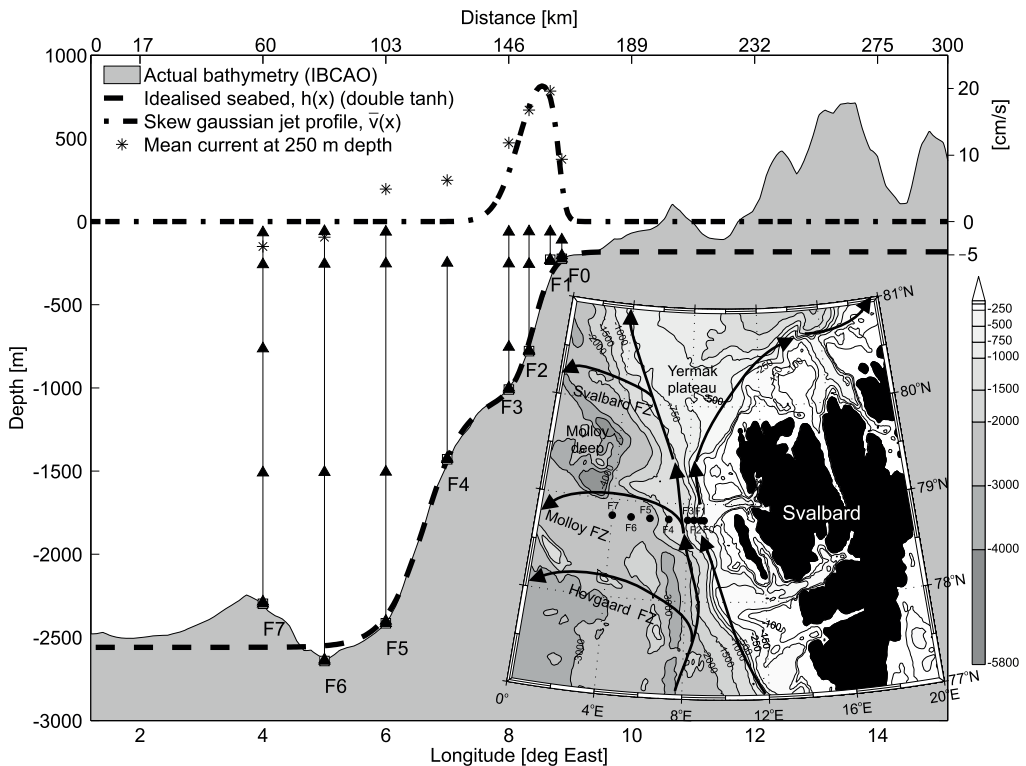[3]Department of Mathematics, University of Oslo, Oslo, Norway.

Figure 1. The geographical positions of the current meter moorings are shown in the map. Bathymetry is based on the International Bathymetric Chart of the Arctic Ocean [*Jakobsson et al.*, 2008]. The WSC circulation system is sketched with arrows (on the basis of work by *Gascard et al.* [1995] and *Walczowski and Piechura* [2007]). Actual bathymetry (gray) along the mooring section and idealized shelf profile, $h(x)$, are shown. Moorings and current meter positions are marked with vertical lines and solid triangles, respectively. The mean northward current at 250 m depth is plotted at each mooring. A skew Gaussian current profile fitted to the mean current data is also shown.

presence of eddies advecting water masses from the warm core of the WSC to the surface along tilting isopycnals has been postulated as a vital mechanism for cooling the current [*Boyd and D'Asaro*, 1994]. Although various sources of the eddies observed in the Fram Strait have been suggested [*Johannessen et al.*, 1987], the formation process and heat loss contribution of these eddies are largely unknown.

[3] The upper slope branch of the WSC can be described as a topographically guided barotropic jet flowing along contours of planetary potential vorticity f/h (where f is planetary vorticity and h is water depth) and is referred to here as the barotropic WSC branch. On the basis of repeated conductivity-temperature-depth (CTD) sections across the shelf edge front, *Saloranta and Svendsen* [2001] found that there is no subsurface density front associated with the Arctic temperature-salinity front on the West Spitsbergen shelf and concluded that barotropic rather than baroclinic instability was responsible for cross-frontal exchange between the WSC

and the shelf waters. However, in a recent study, *Tverberg and Nøst* [2009] report observations of variable horizontal density gradients on the continental shelf. Using a numerical model, they demonstrate that the observed density differences are likely to give rise to frontal instabilities. Earlier studies comment on the distinct low-frequency variability displayed by the WSC. *Hanzlick* [1983] detected signals of periodicity 4–6 days in the power spectrum of the across-shelf current component and attributed them to baroclinic instability processes. On longer time scales, *Morison* [1991] observed a peak at a 19 day period in spectra of bottom pressure. *Cottier et al.* [2005] argued that pockets of AW within Kongsfjorden in northwestern Svalbard were remnants of water that had entered the shelf because of shear instability in the WSC. *Nilsen et al.* [2006] found that topographical waves enhanced by the diurnal tides could add significantly to the heat loss of the WSC, on the same order of magnitude as the winter values of *Saloranta and Haugan*

Table 1. Overview of Moorings F0–F3 Over the Upper West Spitsbergen Slope[a]

	Mooring			
	F0	F1	F2	F3
Latitude (dd.mmm)	78.833	78.834	78.835	78.834
Longitude (dd.mmm)	8.864	8.674	8.329	8.001
Model position (km)	164	160	153	146
Water depth (m)	224	229	779	1010
Deployment date	11 Sep 2007	12 Sep 2007	28 Sep 2007	28 Sep 2007
Retrieval date	11 Sep 2008	5 Jul 2008	5 Jul 2008	5 Jul 2008

[a]Overview includes position, depth, and deployment and retrieval data. The corresponding grid positions used in the linear stability model are also given.

[2004]. *Nilsen et al.* [2006] investigated the influence of neutrally stable vorticity waves, while the present study is focused on unstable modes caused by barotropic instability.

[4] In this paper, current meter data from a mooring array across the eastern Fram Strait are analyzed with the aid of a linear perturbation method for determining eigenmodes of shelf slope currents. In section 2, the data set and the background theory of the linear stability analysis are outlined. Results from applying the linear stability model to the WSC are presented in section 3. An identification of several episodes that match the unstable eigenmodes predicted by the perturbation model was made with wavelet, coherence, and complex demodulation analyses and is also described in section 3. The characteristics of the unstable modes are utilized in section 4 for a more detailed examination of their existence and discussion of their implications for the heat loss and water mass exchange across the oceanic Arctic front on the shelf. In section 5, the main conclusions of the paper are outlined.

2. Data and Methods

2.1. Current Meter Data

[5] The analysis is based on data from an array of current meter moorings across the eastern Fram Strait [*Schauer et al.*, 2004], where the focus is on the three easternmost moorings (F1, F2, and F3) covering the upper West Spitsbergen Slope (WSS) region shallower than 1000 m depth. The positions of the moorings can be seen in Figure 1. The mooring section has been maintained by the Alfred Wegener Institute since 1997 as part of the European Union projects Variability of Exchanges in the Northern Seas (VEINS) (1997–2000), Arctic-Subarctic Ocean Flux Array for European Climate: North (ASOF-N) (2002–2005), and Developing Arctic Modeling and Observing Capabilities for Long-term Environmental Studies (EU-DAMOCLES) (from 2006). Within the International Polar Year project Integrated Arctic Ocean Observing System (iAOOS) Norway, an additional mooring (F0) was installed in September 2007. This mooring, deployed 4 km east of F1, extends the mooring array onto the West Spitsbergen shelf. The present study concentrates on the 2007–2008 deployment year because of the enhanced mooring coverage provided by F0. In Table 1, a summary of the moorings is given. Descriptions of moorings F1–F3 can be found in work by *Fahrbach et al.* [2003] and *Schauer et al.* [2004, 2008]. Table 2 lists the details of mooring F0. Only data from the instruments at the 100 and 200–250 m

levels (the common instrument depths of the four moorings) were used in the analysis of unstable modes.

[6] In Figures 2a–2d, progressive vector diagrams of the measured current at the 200–250 m level of F0–F3 are plotted. This is the approximate depth of the warm core of AW in the barotropic WSC branch. The current displays a relatively steady north–northwest flow, generally aligned with the isobaths. The strongest current is measured at F1, where the current speed exceeds 0.5 m s^{-1} on several occasions throughout the winter months. The asymmetric tendency of the mean current profile is evident, with the current being stronger on the offshore side (F2) of F1 than on the onshore side (F0). Note that the measurement record at F0 is well over 2 months longer than at F1–F3 and that F0 is only 4 km east of F1, whereas F2 is 7 km west of F1. The flow at the deeper moorings F2 and F3 displays more directional variability than the flow at F0 and F1, which is close to rectilinear. For all moorings, the fastest flow is observed during January. In January, the flow is also relatively broad, implying a substantial transport. All moorings seem to undergo a seasonal cycle with fast flow during winter and more moderate current speeds during summer and fall. This cycle is most pronounced at F0. F3 has very low current speed in December, February, and April compared with the other locations. The temperature undergoes a seasonal cycle, with a maximum appearing in November and December at all moorings. The maximum temperature is observed at F2. For the first part of the measurement record, the temperature is quite similar at all moorings, but in January, the temperature at F0 and F1 starts to cool more rapidly than the temperature at F2 and F3. For the rest of the spring and early summer, the temperature stays 1.0°C–1.5°C colder at F0 and F1 than at the moorings farther off-

Table 2. Details of Mooring F0 at Position 78.833°, 8.864°[a]

Instrument	Depth (m)	Sample Interval (s)	Parameters
Sea-Bird MicroCAT SBE 37	89	900	*T, S, p*
Aanderaa RCM 9	117	3600	*u, v, T, S, p*
Sea-Bird MicroCAT SBE 37	150	900	*T, S, p*
Aanderaa RCM 9	205	3600	*u, v, T, S, p*
Nortek Continental ADCP	216	3600	*u, v, T, p*

[a]Parameters: *u*, eastward velocity; *v*, northward velocity; *T*, temperature; *S*, salinity; *p*, pressure. The ADCP readings were influenced by acoustic leakage along the mooring line, rendering the *u* and *v* profiles unusable.
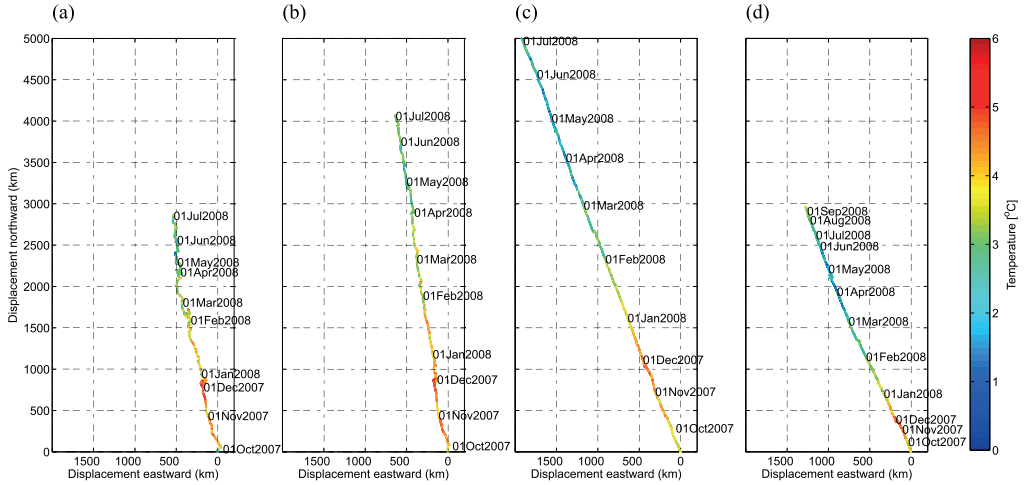
Figure 2. Progressive vector diagrams for the current at the 200–250 m level at (a) F3, (b) F2, (c) F1, and (d) F0. The associated temperature record is plotted in color.

shore. The minimum temperature is observed in late April and early May.

2.2. Linear Stability Analysis

[7] The mean potential vorticity (PV) $\overline{q}$ of a steady, along-shelf current $\overline{v} = \overline{v}(x)$ on an f plane is given by

$$\overline{q} = \frac{f_0 + \frac{d\overline{v}}{dx}}{h}. \tag{1}$$

Here f_0 is the constant Coriolis parameter. The coordinate system is oriented with the x axis pointing east toward the shore and the y axis pointing north along the shelf. If unstable waves exist, $\overline{q}$ has at least one local extremum within the domain [*Mysak*, 1980].

[8] A numerical linear stability analysis of barotropic flows was applied in order to evaluate whether favorable conditions for unstable shelf modes exist in the WSS area. A short outline of the method is given here (for more details see *Gjevik* [2002]). Comparisons have previously been made between the linear perturbation model and numerical ocean models [*Thiem et al.*, 2006; *Davies et al.*, 2003], showing good agreement. The same model was also applied by *Nilsen et al.* [2006] in the study of stable modes in the West Spitsbergen Current.

[9] We assume small perturbations to a steady, geostrophically balanced along-shelf current jet $\overline{v}(x)$:

$$\begin{aligned} u &= u', \\ v &= \overline{v} + v', \\ \eta &= \overline{\eta} + \eta', \end{aligned} \tag{2}$$

where u' is the perturbation in the across-shelf direction (pointing east toward the shore), v' is the perturbation in the along-shelf direction (pointing north along isobaths), and η' is the perturbation of the sea surface displacement. Here $\overline{\eta}$ represents the sea surface displacement of the geostrophi-

cally balanced background field. We then insert equation (2) into the linearized shallow-water equations, restricting ourselves to search for normal modes of the form

$$\begin{aligned} u' &= \hat{u}(y)\cos(kx - \omega t), \\ v' &= \hat{v}(y)\sin(kx - \omega t), \\ \eta' &= \hat{\eta}(y)\cos(kx - \omega t). \end{aligned} \tag{3}$$

Here k is real wave number, t is time, $\omega = \omega_r + i\omega_i$ is complex angular frequency, and the complex phase speed $c = c_r + ic_i = \frac{\omega}{k}$. This results in a set of equations, which, together with the boundary conditions and discretization of the background current and shelf profiles, can be expressed as a matrix eigenvalue problem for ω. For complex ω, the solution is unstable with growth rate (e-folding time) $\gamma = 1/\omega_i$ and wave period $P = 2\pi/\omega_r$. In the case of instability, the amplitude of unstable perturbations will grow by a factor of $\exp(\omega_i t)$. For the unstable modes, $\hat{u}$, $\hat{v}$, and $\hat{\eta}$ become complex functions.

[10] The modeled WSS topography is uniform in the along-shelf direction, and the undisturbed water depth, $h(x)$, is represented by a smooth double tanh function in the across-shelf direction (resolving the two-step nature of the slope; see Figure 1):

$$\begin{aligned} h(x) = {}& a_1\{1 - g_1\tanh[-(x - x_1)/s_1]\} \\ & + a_2\{1 - g_2\tanh[-(x - x_2)/s_2]\} \\ & - a_2(1 - g_2), \end{aligned} \tag{4}$$

where $a_1 = 621$ m, $g_1 = 0.7069$, $x_1 = 117$ km, $s_1 = 7$ km, $a_2 = 2350$ m, $g_2 = 0.3191$, $x_2 = 155$ km, and $s_2 = 14$ km. This is the same bathymetric function as was used by *Nilsen et al.* [2006]. The maximum upper bottom slope is $\sim 6 \times 10^{-2}$ and somewhat steeper than the maximum deep bottom slope ($\sim 5 \times 10^{-2}$). The more gently sloping segment between the two slopes is $\sim 1 \times 10^{-2}$.
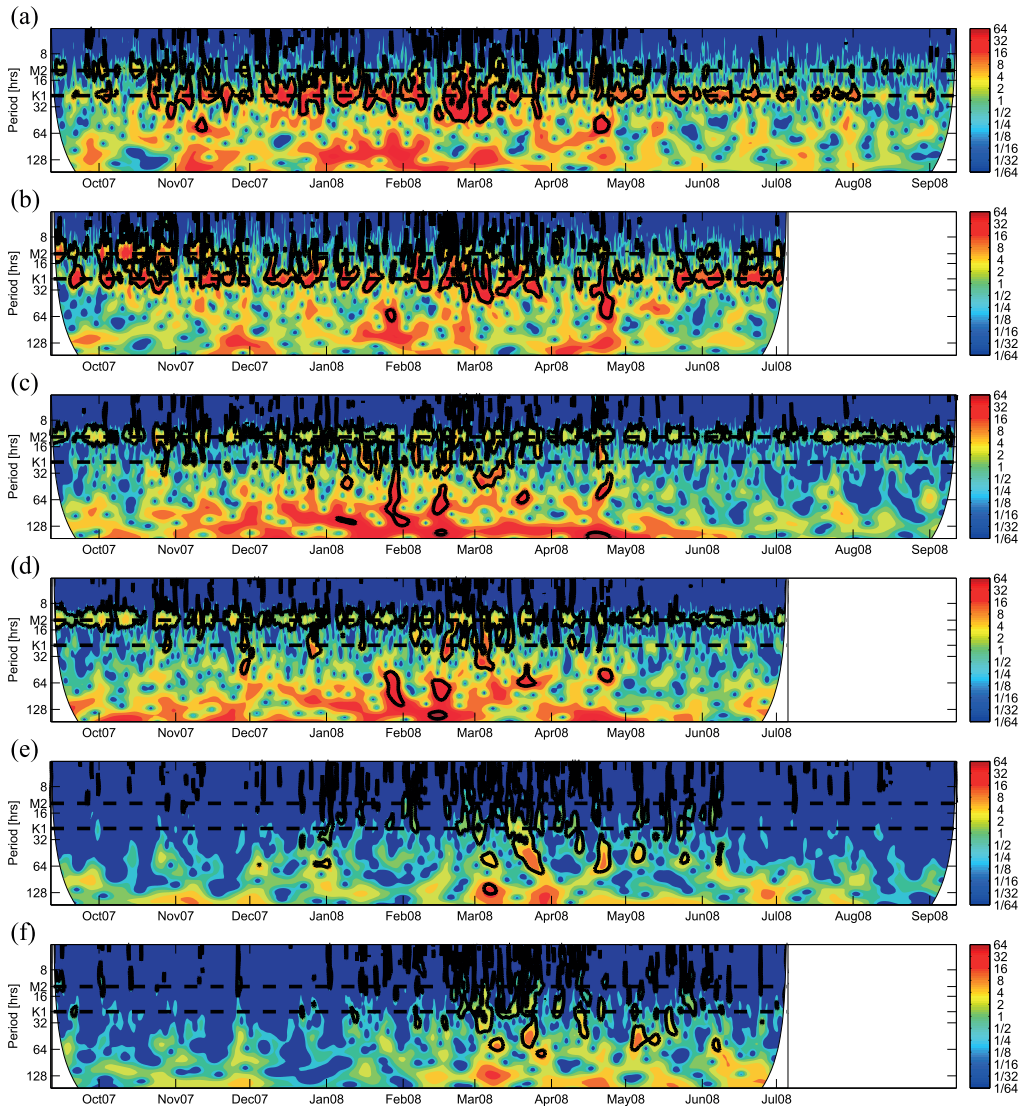
Figure 3. Wavelet power spectra of (a) u at F0, (b) u at F1, (c) v at F0, (d) v at F1, (e) T at F0, and (f) T at F1 from the current meters at the 200–250 m level throughout the deployment period in 2007–2008. The power is normalized by the variance $1/\sigma^2$. The periods of M2 (12.42 h) and K1 (23.93 h) are indicated by dashed lines. Regions with power above the 95% confidence level are enclosed by black contours.

[11] Analyses of the current meter data suggest that the current is asymmetrical, with a sharper current shear on the shore side than on the ocean side (Figure 1). Transects across the West Spitsbergen Current taken with ship-mounted acoustic Doppler current profilers (ADCPs) [*Walczowski et al.*, 2005] also support this idea. An asymmetric (but still differentiable) idealized current profile, $\bar{v}(x)$, is therefore proposed. This current profile is constructed by multiplying a Gaussian profile with a sigmoid curve, yielding a skew Gaussian profile given by

$$\bar{v}(x) = \frac{\bar{v}_{\max} \exp\left\{-\left[\frac{2(x-L_B)}{B}\right]^2\right\}}{1 + \exp\left[\frac{x-L_B-B/r}{B/s}\right]}. \quad (5)$$

Table 3. Variance of Different Period Bands for Along-Shelf and Across-Shelf Velocity at the 200–250 m Level at Moorings F0–F3

	Across-Shelf Velocity, u				Along-Shelf Velocity, v			
	F0	F1	F2	F3	F0	F1	F2	F3
Total variance (cm^2 s^{-2})	42	40	64	135	94	130	278	215
Variance as percentage of total variance (%)								
Long-periodic mesoscale, 120 h to 14 days	8	6	19	27	16	17	26	16
Short-periodic mesoscale, 64–120 h	6	5	19	22	8	8	7	9
Superdiurnal, 32–64 h	12	11	18	13	6	6	4	5
Diurnal, 20–32 h	23	28	10	5	4	5	3	3
Inertial/semidiurnal, 11–14 h	6	12	3	1	8	8	3	3
Short periodic, <11 h	7	9	4	2	3	3	1	1

Here $\bar{v}_{max}$ is the maximum current speed, L_B is the position of the maximum of the Gaussian basis function, B is the half width of the Gaussian, and $L_B - B/r$ is the position where the sigmoid part is exactly 0.5. Furthermore, r and s are parameters controlling the steepness and width scale of the sigmoid curve. These parameters were manually tuned to the values $r = 2$ and $s = 10$ by comparison with the mean observed current (Figure 1) at the 200–250 m level of F0–F3. The skew Gaussian profile deviates from the observed profile at moorings F4–F7 (also shown in Figure 1). However, these current meters are assumed to be situated inside the offshore, deeper-slope branch of the WSC, which is supported by low correlation with the upper slope moorings. The half width on the shelf side of the current profile will naturally be narrower than the half width on the offshore side (B). For later reference, the half width on the shelf side, b, is defined as the distance from the current maximum to the point on the shelf side where the current amplitude is reduced to half of the maximum value.

[12] The relative amplitude of the perturbation current versus the background current is not determined through the eigenvalue calculation. In order to make both the perturbation and background currents discernable in a vector plot of the modal structure, a scaling is introduced. The scaling is according to

$$u = \kappa u'$$
$$v = \bar{v} + \kappa v',$$

where

$$\kappa = \alpha \frac{\bar{v}_{max}}{\hat{v}_{max}}. \qquad (6)$$

Here α is a scaling factor and $\hat{v}_{max}$ is the maximum of the normalized along-shelf current $\hat{v}$ obtained through the eigenvalue analysis. In the present study, a value of $\alpha = 0.4$ was found to adequately scale the perturbation and background current fields for plotting purposes.

[13] The width of the calculation domain is $L_x = 300$ km. The lateral boundary conditions at $x = 0$ and $x = L_x$ were zero normal velocity, i.e., $u' = 0$. A grid size of $\Delta x = 1$ km proved to be sufficient for numerical convergence, provided that the current profile has a smooth derivative. Calculations were made for wavelengths in the range 10–100 km, with intervals of 1 km.

[14] It is impossible to determine the complex phase speed $c = c_r + ic_i$ of the unstable modes of an arbitrary current profile analytically. Still, it is feasible to obtain theoretical bounds on c_r and c_i. *Howard* [1961] derived a semicircle theorem, giving bounds on phase speed, c_r, and growth rate, c_i,

of unstable waves on a barotropic shear flow on an f plane in a flat-bottomed channel. The semicircle is given by

$$(c_r - \bar{v}_{min})^2 + c_i^2 \leq (\bar{v}_{max} - \bar{v}_{min})^2, \qquad (7)$$

where $\bar{v}_{max}$ and $\bar{v}_{min}$ are the maximum and minimum flow speeds within the domain. This was later extended by *Collings and Grimshaw* [1980] and *Hall* [1980] to account for topography. Other versions, which include the beta effect and stratification, have also been developed [e.g., see *Pedlosky*, 1987, chapter 7.5]. The results for barotropic shelf waves are summarized by *Collings and Grimshaw* [1984].

3. Results

3.1. Wavelet and Variance Analysis

[15] In an attempt to capture the nonstationary and transient nature of the unstable wave modes, wavelet analysis [*Torrence and Compo*, 1998] was applied to the data set. Wavelets have previously been used in the analysis of vortex-like instabilities in current meter data [*Lilly et al.*, 2003; *Davies et al.*, 2008]. Described as a plane wave, the Morlet wavelet, focused in time by Gaussian damping, was chosen as the mother function. Figures 3a–3f show wavelet power spectra of the across-shelf (easterly) current, along-shelf (northerly) current, and temperature at the 200–250 m level of F0 and F1. The diurnal tide is most energetic in the across-shelf current component (Figures 3a and 3b), whereas the semidiurnal tide dominates in the along-shelf current component (Figures 3c and 3d). Both tidal components show up with significant wavelet power throughout the year. Energy around the diurnal period is enhanced during winter. Single episodes with significant power for low-frequency oscillations (with longer period than K1) are observed at both moorings, almost exclusively during winter and spring. These episodes appear simultaneously at the two moorings, indicating that they reflect oscillations with a spatial extent that accommodates both moorings. For the temperature (Figures 3e and 3f), episodes at significant wavelet power only occur during winter and spring, possibly because the temperature gradients are stronger then, leaving a signal that is easier to detect.

[16] In Table 3, the variance of the band-pass-filtered signals of u and v have been compared to the total variance at moorings F0–F3 for the 200–250 m level. The total variance is 2–3 times larger in v than in u for all moorings and is increasing in the downslope direction. The variance at the two shallowest moorings (F0 and F1) is dominated by diurnal oscillations in the across-shelf velocity component, whereas the deeper moorings are more influenced by long-
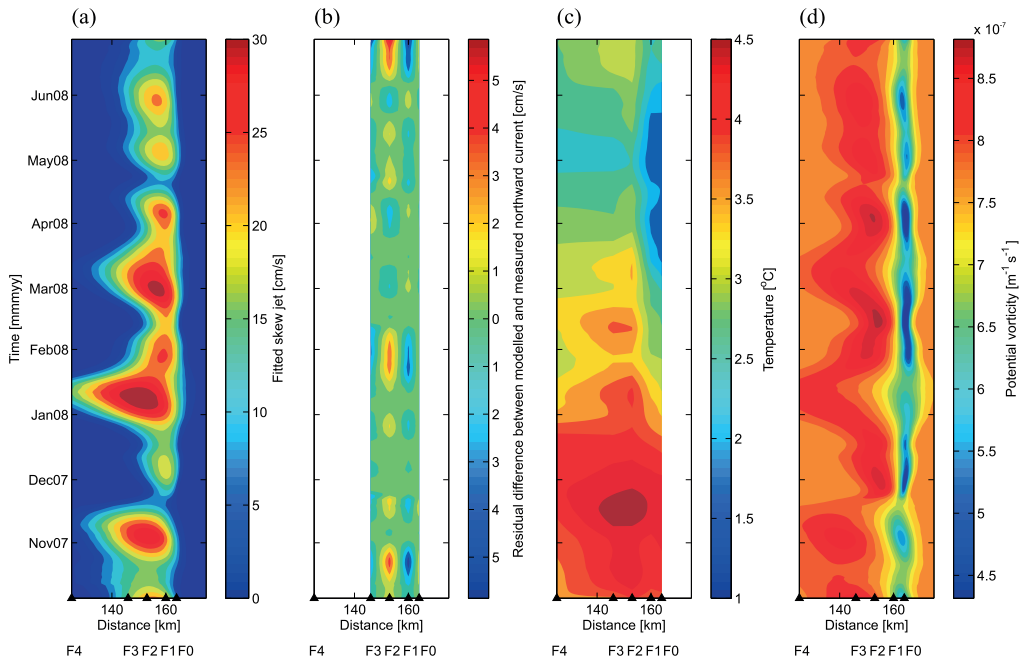
Figure 4. Hovmöller diagrams of (a) fitted skew jet profile, $\bar{v}$ (cm s^{-1}), (b) residual difference (cm s^{-1}) between the fitted profile and the observed smoothed (14 day running mean) profile at F0–F3, (c) observed temperature (14 day running mean) at the 200–250 m level at F0–F4, and (d) potential vorticity (m^{-1} s^{-1}) calculated from the fitted current profile.

periodic oscillations. In the along-shelf velocity component, the semidiurnal tide accounts for more variance than the diurnal, at the shallow moorings, but long-periodic oscillations (120 h to 14 days) are most important. This tendency is even clearer for the deep moorings, where long-periodic oscillations also dominate in the across-shelf direction. The fact that the diurnal tide is clearly dominating in the across-shelf component for upslope moorings in the Fram Strait has previously been established from analysis of current measurements by *Kasajima and Svendsen* [2002]. Increased variance in the across-shelf component could be an indication of shelf waves generated by the diurnal tide.

3.2. Results From the Linear Stability Analysis

[17] The northward current component from the 250 m level at F0–F3 was smoothed with a 14 day running mean and was subsampled to daily values. This slowly varying smoothed time series was assumed to be a fair representation of the background current profile. For each time step, a skew jet profile (5) was numerically fitted to the data. The currents farther in on the shelf ($x = 200$ km) and far offshore ($x = 50$ km) were set to zero. The values of the parameters $\bar{v}_{max}$, L_B, and B were found by minimizing the least squares difference between the fitted profile and the smoothed data series. Figure 4a shows the time evolution of the fitted background current profile, $\bar{v}(x)$. The mean position of the maximum current is ~157 km, or halfway between F1 and

F2, whereas the mean offshore half width is $B = 15$ km, corresponding to a shelf-side half width of $b = 7$ km. Episodes of high current speeds occur throughout the year but are mostly concentrated between early January and mid-April. The accompanying time series of residual difference between the fitted profile and the smoothed data from moorings F0–F3 is also shown (Figure 4b). The maximum mismatch between observed (smoothed) and modeled currents occurred at the end of the time series, when the modeled current at F2 and F1 differed by 0.05–0.06 m s^{-1} from the observed current. The mean relative residual between the observed and modeled currents was ~5%. The temperature at the 200–250 m level of moorings F0–F4 is plotted in Figure 4c and shows that the position of the hot core of the WSC varies between F2 and F3. By the end of March, the temperature at both F0 and F1 had cooled below 3°C, which is the commonly used lower temperature limit defining Atlantic water in the Nordic seas. Figure 4d shows potential vorticity, $\bar{q}(x)$, calculated from equation (1). Episodes of strong maxima or minima in modeled potential vorticity are related to high horizontal shear, caused by a growing maximum in the modeled current speed and/or a narrowing of the half width.

[18] The linear stability analysis was then carried out on the fitted current profile (Figure 4a) for each time step, arriving at a time series of stable and unstable modes. The most unstable conditions occurred on 17 February 2008. Maximum speed, $\bar{v}_{max}$, offshore half width, B, and position
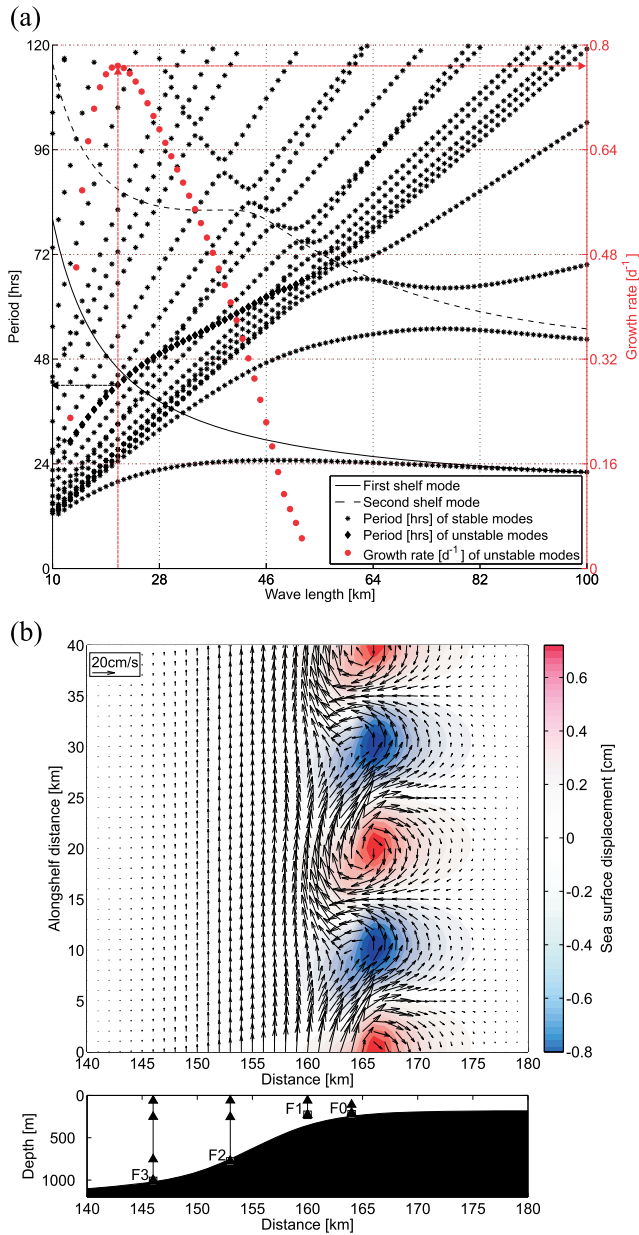
(a)

(b)

Figure 5. (a) Dispersion diagram from linear stability analysis of the fitted profile that results in the highest growth rate. The periods of both stable (black asterisks) and unstable (black diamonds) modes are shown. The associated growth rate of unstable modes is shown with solid red circles. The first and second shelf modes (with no background current) are also shown. The period and growth rate of the fastest growing unstable mode are indicated with arrows. (b) Modal structure of the unstable wave mode with the highest growth rate. The background and perturbation flow fields (scaled as in equation (5)) are shown with black vector arrows. The perturbation sea surface displacement is plotted in red and blue.
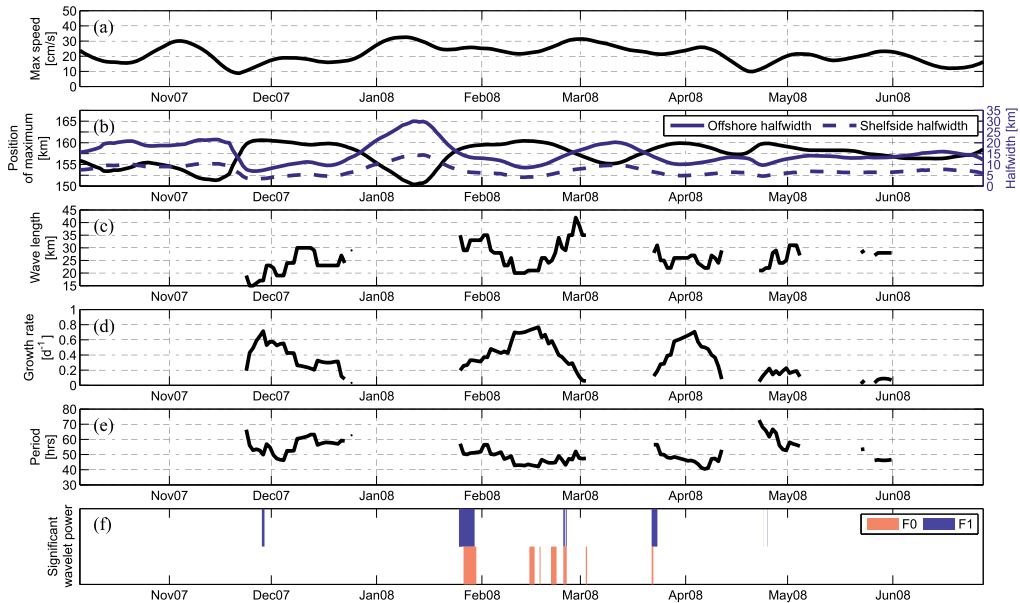
Figure 6. Time series of unstable events. (a) The maximum speed of the fitted current profile. (b) The position and half widths of the fitted profile. (c–e) The wavelength, growth rate, and period of the gravest unstable mode, respectively. (f) Intervals where the period of the unstable mode matches a period with significant wavelet power in u or v at either F0 or F1, indicated with red or blue, respectively.

of the fitted skew jet, L_B, were then 0.23 m s^{-1}, 9 km, and 160 km, respectively. In Figure 5a, the detailed dispersion relation from the linear stability analysis of these conditions is presented. A multitude of discrete bands of both stable and unstable modes can be seen. For long wavelengths, the two lowest stable modes approach the first and second shelf modes (i.e., the two lowest modes in the absence of a mean current). The unstable modes appear as a single band of higher modes between 14 and 52 km wavelength, with a single peak in growth rate (the red curve). The peak in growth rate is $\gamma = 0.77$ per day. The corresponding wavelength was quite short, ~20 km. The associated wave period is ~40 h. In Figure 5b, the modal structure associated with the most unstable mode is shown. The center of the vorticity wave is located at the shelf break, a few kilometers east of F0. This proved to be the typical position of the most unstable mode for all the modeled events.

[19] The detailed time series of the fitted current jet parameters (maximum current amplitude, localization, and offshore and shelf-side half widths) are plotted in Figures 6a and 6b. Assuming that the unstable mode with the highest growth rate most likely will dominate and hence show up in the observations, the time evolutions in wavelength, wave period, and growth rate of the gravest mode for the entire measurement record are displayed in Figures 6c–6e. The scale-averaged wavelet spectrum [*Torrence and Compo*, 1998] of u and v was calculated for a ±10% band around the wave period of the gravest mode for moorings F0 and F1. The resulting power is compared with the 95% confidence

level corresponding to a red noise background process. Figure 6f indicates the time intervals when the oscillation period of the gravest unstable mode steps out with significant power in the scale-averaged wavelet spectra of u and v at F0 and F1. Unstable conditions prevail 40% of the time. The mean wavelength of the most unstable mode was 26 km, the mean period was 52 h, and the mean growth rate was 0.36 d^{-1}.

3.3. Sensitivity Analysis of Jet Stability

[20] The crucial parameters of the skew Gaussian jet (i.e., position, L_B, half widths, B and b, and magnitude, $\bar{v}_{max}$) were systematically varied in order to investigate their influence on the stability of the current profile. In Figure 7a, the results for positions 145–165 km and maximum current speeds between 0.0 and 0.3 m s^{-1} are shown. The Gaussian half width of the current is kept constant at $B = 10$ km (this corresponds to a half width of $b = 4.5$ km on the shelf side). High current speeds are associated with increasing wavelength and more rapid oscillations (decreasing period) of the fastest growing unstable wave. On the other hand, if a given current maximum is shifted to the steeper part of the slope, both the period and the wavelength will decrease. There is a local maximum in growth rate of the gravest unstable mode when the current maximum is situated close to the shelf break, whereas over the steeper part of the slope (around the position of F2) the current is unstable only at high current speeds ($\bar{v}_{max} > 0.17$ m s^{-1}). This is in accordance with the numerical study carried out by *Poulin and*
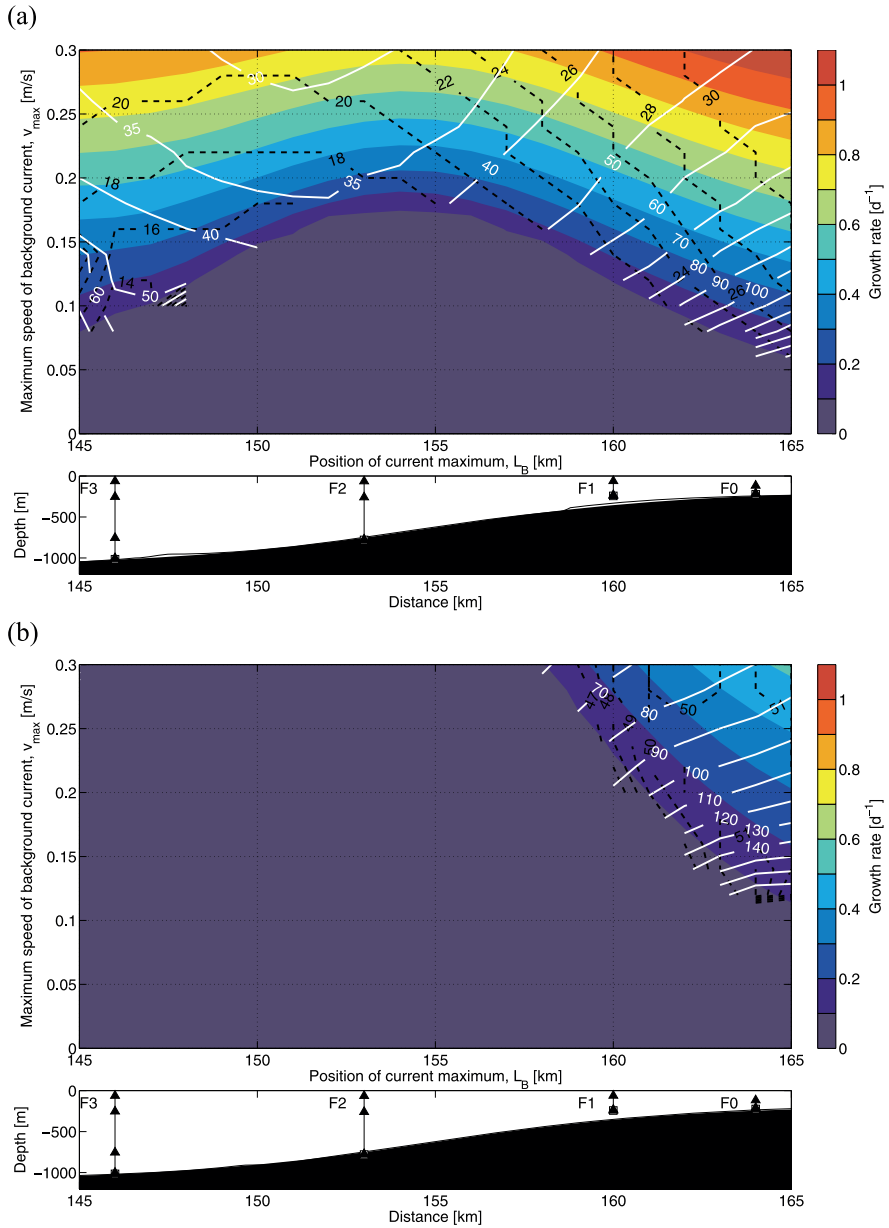
Figure 7. Sensitivity study with variable magnitude and position of the current maximum. The half width B is kept constant at (a) 10 and (b) 18 km. The growth rate of the gravest unstable mode is plotted with colored, solid contours. The corresponding period and wavelength of the gravest unstable mode are displayed with solid white and dashed black contour lines, respectively.
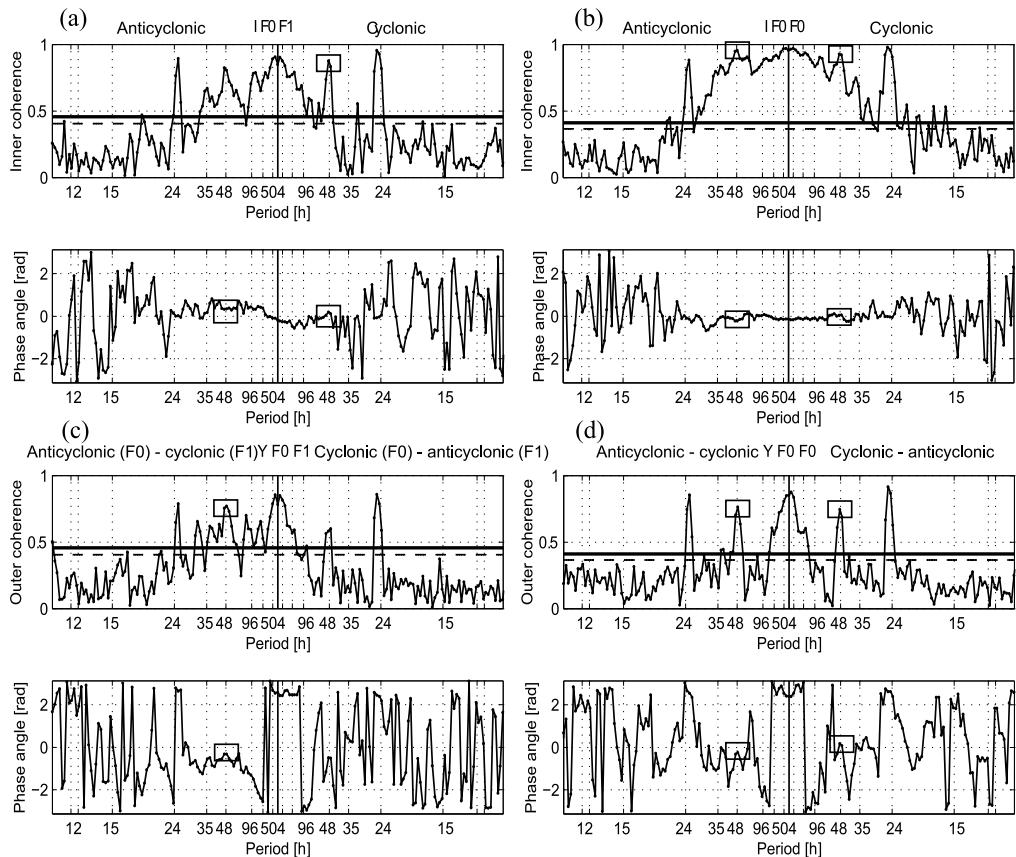
Figure 8. (a) Inner and (c) outer coherence spectra between current meters at the 205 m level at F0 and the 233 m level at F1, given as a response of F0 to F1. To examine the barotropic assumption, vertical (b) inner and (d) outer coherences between the 117 and 205 m levels at F0 are given. Periods of particular interest are highlighted by rectangles. See text for further details.

Flierl [2005], who showed with a similar linear model that for low Rossby numbers and steep prograde (with the shallow water to the right) topography, the slope acts to stabilize the flow. In Figure 7b, the offshore half width of the current is kept constant at $B = 18$ km (this corresponds to a half width of $b = 8$ km on the shelf side). The broadening of the flow has dramatic consequences for the stability of the current, which grows unstable only at high current speeds and a maximum current shoreward of F1.

3.4. Spatial Coherence and Complex Demodulation

[21] Inner and outer rotary spectra [*Livingstone and Royer*, 1980] for the current time series are calculated in order to study rotating current vectors. The inner spectral functions describe corotating components, and the outer functions describe counterrotating components. The same applies to the rotating phase spectra. Figure 8 shows the inner and outer coherence spectra between current meters at F0 and F1

at 205 and 233 m depth (Figures 8a and 8c) and the inner and outer coherence spectra between the two current meters at F0 at 117 and 205 m depth (Figures 8b and 8d). On the basis of the time series of unstable events (Figure 6e), we focus on rotational cyclonic and anticyclonic components for periods around 52 h (the mean period of the unstable modes from the stability analysis in section 3.2). In general, we should expect an elliptical hodograph with variable orientation of the major axis for these periods. An ellipse-shaped hodograph can be constructed from two counter-rotating circular components with different radii and phase differences for cyclonic and anticyclonic rotation. This is an important aspect when interpreting coherence spectra; that is, two rotating ellipses will show up with coherence energy for both cyclonic and anticyclonic rotation.

[22] Results important to our study are highlighted with black rectangles in Figure 8. The rotational energy around 48 h shows up as a robust estimate, high above the 95%

confidence level. Figures 8a (bottom) to 8d (bottom) show the phase angle differences between the rotating components, and the $P = 48$ h angles marked by the rectangles indicate a 1–2 h time delay between the rotating signals. The main results from Figure 8 are that the horizontal coherences in Figures 8a and 8c depict two rotating vectors within the same vorticity field and that the vertical coherences in Figures 8b and 8d depict a barotropic structure. The latter is also true for F1 (not shown). The 1–2 h time delay may reflect that the mooring section is not strictly parallel to the across-slope direction and that current meters will therefore record data displaced in the along-slope direction within the northward propagating vorticity field.

[23] Figure 8a indicates that the current vectors at 250 m have a tendency to corotate cyclonically at F0 and F1 for $P = 48$ h, but there is also coherence energy in the anticyclonic component since the hodograph is an ellipse. Results from the counterrotating analysis (Figure 8c) show a likely anticyclonic rotation velocity vector at F0 ($P = 48$ h) when there is a cyclonic rotation at F1.

[24] To determine how signal characteristics at specific frequencies change throughout the duration of the time series, complex demodulation [e.g., *Emery and Thomson*, 2001] is used. This method determines the amplitude and phase and thus the ellipse orientation of the cyclonic and anticyclonic rotating components of the velocity time series. The complex demodulation uses least squares function fitting, which seeks to determine an optimal function as a linear combination of any specified basis functions for each measuring point such that the quadratic difference between the estimated value and the observed value is minimized [e.g., *Press et al.*, 1992]. Here the least squares function fitting was solved by use of singular value decomposition (SVD) [e.g., *Press et al.*, 1992]. The demodulated signal was found and tested for sequential segments of different lengths. In order to produce a time series that resolves the $P = 48$ h component for further analysis, a 480 h window function was run over the current data with 10 h separation (or 470 h overlap).

[25] Figures 9a and 9b show that the anticyclonic amplitude is dominating (Figure 9a, top) for the $P = 48$ h period. A measure of the reliability of this signal tracing method is given by a high amplitude in Figure 9a together with a flat phase curve in Figure 9b over two to three cycles of the period given. Hence, Figure 9 indicates that the strongest, least noisy signal is found between January and May for the anticyclonic component with relatively high amplitude and a flat phase curve at $P = 48$ h. The effect of these horizontal oscillations on the heat flux (Figure 9c) will be discussed in section 4.2.

4. Discussion

[26] The barotropic WSC branch leaning against the shelf break is captured by four moorings across the slope (F0–F3 in Figure 1). The current meter data at 200–250 m depth have been used to construct a continuous skewed Gaussian profile (Figure 4) in order to study the barotropic stability (Figure 6) between the jet-like slope-break current and the calm shelf area. Figure 4 shows that the skew jet reproduces the data quite well and that the discrepancies are due to the modeled maximum current positioning itself between cur-

rent meters. Time series of the maximum current position, the maximum current, and the half width of the skewed current profile are parameters inserted into the linear stability model.

[27] Results from the model are given in Figures 6c–6e, showing that the barotropic current profile becomes unstable and produces horizontal vorticity waves with wavelengths between 20 and 40 km and oscillation periods between 40 and 70 h, which have an amplitude growth rate of up to 0.8 d^{-1}. The results are within the constraints of *Howard*'s [1961] semicircle theorem (equation (7)). This is demonstrated in Figure 10, where the time series of real and complex phase speeds are plotted, along with the bounds from the semicircle theorem. The real phase speed comes quite close to its theoretical limit, whereas the complex phase speed (which is directly proportional to growth rate) is less than 10% of its maximum allowable value. The unstable events are controlled by a high Rossby number, although the position of the current jet is also influencing the onset of unstable situations. The Rossby number, Ro, is given by

$$Ro = \frac{\overline{v}_{max}}{f_0(B + b)}. \tag{8}$$

In Figure 11, the time series of Ro is shown. All of the unstable events are associated with peaks in Rossby number (usually $Ro > 0.06$). Situations where a relatively high Rossby number does not lead to unstable conditions occur when the current jet is positioned too far offshore, where the current is under the influence of the stabilizing slope.

[28] Figure 6 indicates that the wavelength and period of the gravest unstable wave mode are determined by the position of the maximum current. Figure 7a gives the result of a sensitivity study with variable magnitude and position of the current maximum with a 10 km half-width skewed Gaussian profile. The 10 km half width is quite representative of the current profiles producing unstable events in Figure 6. As shown by Figures 1 and 4a, the maximum current is often found between F2 and F1 and closest to F1 when the half width approaches 10 km. The sensitivity study (Figure 7a) tells us that the wave period should lie between 40 and 50 h and the wavelength should lie between 20 and 30 km at this location. A relatively high growth rate is seen for current maxima above 0.2 m s^{-1}, and the growth rate increases if the current maximum is shifted eastward. This is explained by a less stabilizing topography when the profile is approaching the flat shelf areas. On the basis of the 2007–2008 data, the current maximum seems to be topographically trapped between F2 and F1 and never east of F1.

[29] A necessary (but not sufficient) criterion for instability is that the mean potential vorticity has a local extremal value (equation (1)). This criterion agrees with the time series of PV (Figure 4d), which shows a strong local minimum around F0 when the model indicates generation of unstable wave modes (Figure 6). The highest growth rate and thus the most unstable situation is found in mid-February when the PV time series in Figure 4d has its global minimum. This event is connected to a narrow current profile with large negative relative vorticity over the shelf break, while the modest northward velocity in this period lies around the average of the time series.
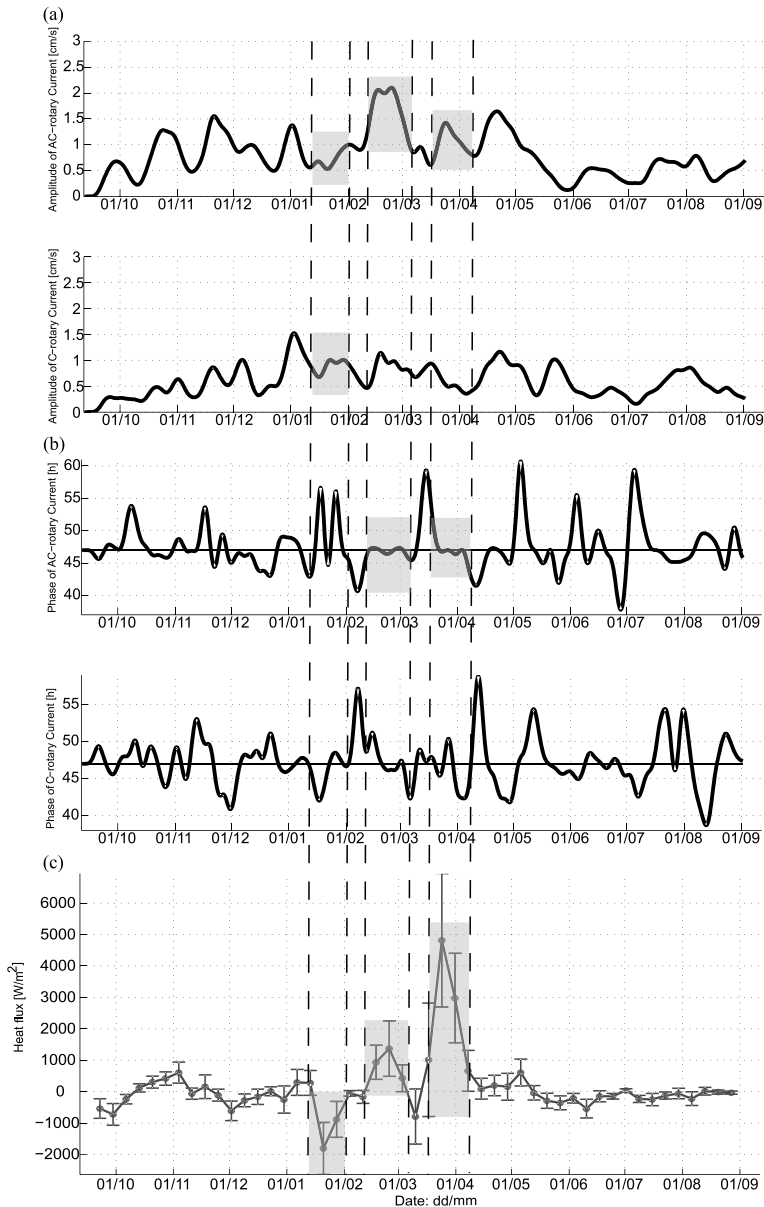
Figure 9. Complex demodulation of current meter data at F0 (250 m level) into (top) anticyclonic and (bottom) cyclonic rotating components showing (a) amplitude and (b) phase change for the 48 h wave period. The phase change has been converted to wave period for both anticyclonic and cyclonic components by $P_{new} = 2\pi/(\omega_{48h} - d(\text{phase})/dt)$. (c) On the basis of the wave signal at $P = 48$ h, a time series of the horizontal heat flux (W m^{-2}) at F0 is produced. Events of particular interest are highlighted by gray shaded rectangles.
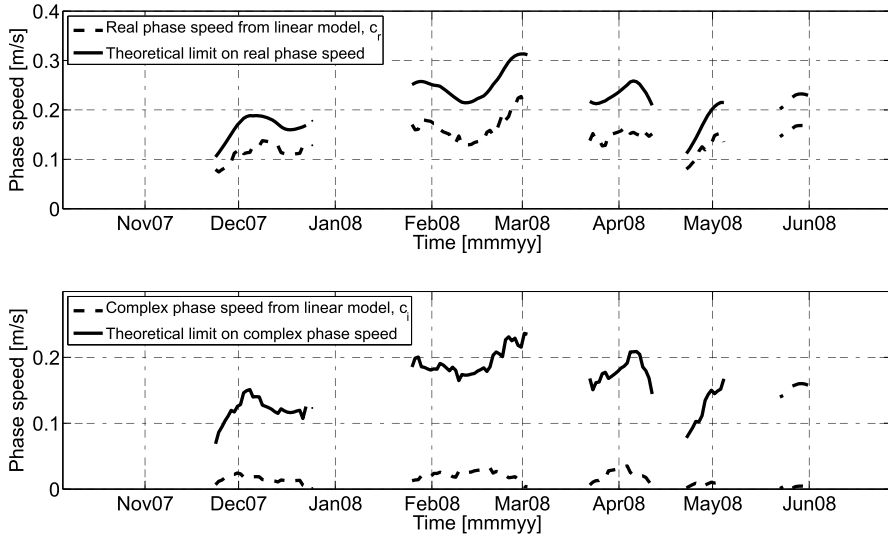
Figure 10. Comparison between (top) real and (bottom) complex phase speeds from the linear stability model and bounds from *Howard*'s [1961] theorem (equation (7)).

4.1. Observed Barotropic Wave Mode

[30] Energy around the 48 h period shows up as a strong and significant signal in both the horizontal and vertical coherence analyses (Figure 8) between F0 and F1 and in different depths on F0. The signal is completely absent in the coherence analysis between F1 and F2 (not shown), which confirms that we are dealing with a shelf break confined oscillating disturbance, a disturbance that lasts long enough to become significant (above the 95% confidence level) in a coherence spectrum. Separating out the 48 h signal in more detail through complex demodulation (Figure 9) shows that the time intervals of significant signal coincide well in time with the unstable wave events determined by the model (Figure 6). The 48 h period is still close to the wave periods which are predicted by the linear stability analysis (mean value $P = 52$ h). The combination of inner and outer coherence spectra, together with complex demodulation of the current meter data at F0, establishes the fact that
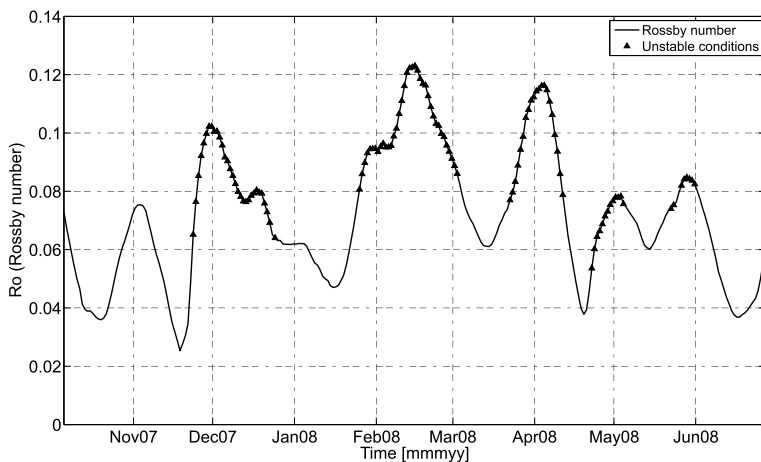

Figure 11. Time series of Rossby number (equation (8)) calculated from the time series of the fitted current profile. Unstable conditions (from the stability analysis) are marked with solid black triangles.

14 of 18

48

we are observing a barotropic wave mode with a period around 48 h and with a horizontal vorticity wave center in the vicinity of F0 (both cyclonic and anticyclonic rotation at F0) but mostly to the west of F0 (dominantly anticyclonic rotation at F0). Figure 8c also shows that there is anticyclonic rotation at F0, while the current vector at F1 rotates cyclonically, confirmed by Figures 9a and 9b. Hence, we expect the vorticity wave center to be positioned around F0 and possibly shifted to the west of F0 for some periods.

[31] The modeled dispersion relation and wave structure for the barotropic vorticity wave mode with the highest growth rate are given in Figures 5a and 5b, respectively. The maximum current for a current profile of 9 km half width is positioned at F1 in mid-February, generating a strong current shear and the time series' minimum PV value at F0 (Figure 4d). Complex demodulation of the 205 m current meter data at F0 captures the event and responds with a 3 week persistent anticyclonic signal at $P = 48$ h (Figures 9a and 9b). As discussed in the previous paragraph, anticyclonic current rotation shows that the current meter is positioned east of a horizontal vorticity wave center. This contradicts the model result in Figure 5b, which shows the mooring to be west of the center. We do not expect the model to replicate the data exactly since the model is based on an idealized bottom topography and a smoothed current profile, while the current meter moorings are placed over a rugged real topography. However, the timing of the barotropic unstable current events (Figures 6 and 9) and the approximate match in oscillation wave period are striking, and we believe that we have managed to capture the dominant dynamics by the idealized linear stability analysis. The model will, in turn, give us the approximate wavelength and thus the dispersion relation of the vorticity waves.

4.2. Heat Loss Estimates

[32] Following the ideas of *Helland-Hansen and Nansen* [1912] and *Boyd and D'Asaro* [1994] that lateral exchange with colder surrounding waters is the primary mechanism for cooling of the subsurface warm core of the WSC, we will estimate the contribution to lateral heat loss [*Nilsen et al.*, 2006] from the gravest unstable wave mode existing along the WSS. We base our estimates on the wave characteristic found in Figures 9a and 9b and extract the oscillating temperature signal ($P = 48$ h) the same way through least squares function fitting by using SVD.

[33] To estimate the heat loss from the upper slope domain, consider the total time derivative of the mean temperature $d\overline{T}/dt$ and the mean heat equation when following a particular parcel of fluid:

$$\rho c \frac{d\overline{T}}{dt} = \rho c \left[\frac{\partial \overline{T}}{\partial t} + \overline{v} \frac{\partial \overline{T}}{\partial y} \right] = -\nabla \cdot \tau, \qquad (9)$$

where ρ is seawater density, c is the specific heat of seawater, the total derivative $d/dt = \partial/\partial t + \overline{\mathbf{v}} \cdot \nabla$, and the velocity field is defined as in (2). Here $\tau = (\tau_u, \tau_v) = \rho c \overline{\mathbf{v}'T'}$ is defined as the mean eddy heat flux, where T' is the perturbation to the mean temperature $\overline{T}$. The perturbations denoted by primes are associated with the gravest unstable wave mode, and $\overline{\mathbf{v}'T'}$ is the cross-correlation function between velocity and temperature, with time averaging over 7 days. The averaging interval is chosen so that it captures a sig-

nificant number of oscillations and at the same time manages to reproduce time variations throughout the seasons. It is difficult to estimate the heat loss of the eddy heat flux in the along-slope direction since there were no upstream or downstream moorings. Assuming that the along-slope term, (τ_v), is small compared to the across-slope term and assuming isopycnal diffusion by vorticity waves only, the heat loss contribution from the across-slope eddy heat flux $\tau_u = \rho c \overline{u'T'}$ can be estimated by using the first term ($\partial/\partial x$) on the right-hand side of (9).

[34] A time series of the horizontal heat flux (W m^{-2}) at F0, based on the rotating wavefield in Figures 9a and 9b and the demodulated temperature signal at the $P = 48$ h oscillating period, is presented in Figure 9c. The first noticeable deviation from zero in the heat flux time series is found in the second half of January. However, no physical interpretation could be done since the phase of the rotating components is inconclusive during this period. The next two large heat flux periods (period 1, mid-February to March; period 2, mid-March to April) are linked to significant signals in the rotating components. On average, the northward flowing water experiences a 1000 W m^{-2} heat loss toward east at F0 within period 1. A cyclonically dominated signal ($P = 48$ h) emerges at F1 over the same time interval (not shown), significant according to the above definitions, and the averaged westward heat flux is calculated to be -2000 W m^{-2}. The same situation with significant rotating components ($P = 48$ h) reoccurs during period 2 but now with dominating anticyclonic rotation at F1 and a heat flux toward east (not shown), which results in $\Delta \tau_u \sim 2500$ W m^{-2} over the 4 km separation between F0 and F1.

[35] Using (9) in an Eulerian way, we will estimate the local change in temperature over periods 1 and 2 due to the unstable vorticity waves. The mean temperature change upstream of the mooring position ($\partial \overline{T}/\partial y$) is estimated using *Saloranta and Haugan*'s [2004] winter averaged along-slope temperature gradient, $-0.31°C$ per 100 km. Multiplied by the average velocity of the WSC, 0.2 m s^{-1}, the advection term in (9) becomes small compared to the heat flux divergence term. Hence, the local rate of change in temperature is given by the east–west divergence in the heat flux in (9), and the heat loss of the water masses below the surface layer is here assumed to be governed solely by isopycnal diffusion due to the unstable vorticity waves ($P = 48$ h). Using the above mentioned approximate differences for the east–west heat flux divergence between F0 and F1 (4 km apart) and allowing the isopycnal diffusion to last for 3 weeks during period 1 and 2 weeks during period 2, we arrive at a temperature reduction $\Delta T \sim -0.2°C$ for both time periods. This corresponds to 50% of the measured temperature reduction during period 1 and 60% during period 2 when examining the 14 day running mean in Figure 4c.

[36] In order to compare with earlier estimates, using hydrographic data along the WSS [*Saloranta and Haugan*, 2004], (9) will be utilized in its original Lagrangian form. We assume the slope profile (4) to be valid along the whole WSS, a distance of ~400 km. By integrating (9) over the box volume encapsulating the upper part of the barotropic WSC branch, hugging the shelf area to the east ($A_{shelf} = 250$ m × 400 km), it is possible to calculate the AW temperature loss by isopycnal diffusion due to the unstable vorticity waves with periods around 48 h (see Figure 12 for
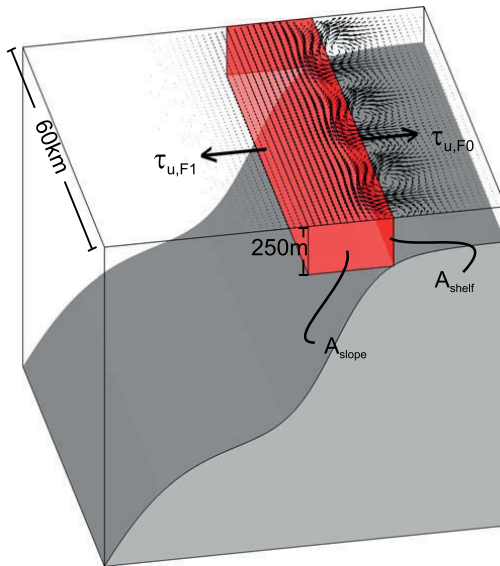
Figure 12. Illustration of box volume for heat flux calculations. The modal structure depicted in Figure 5b is overlaid on the sea surface. Here the along-shelf dimension of the box volume is 60 km. For the calculations an along-shelf dimension of 400 km was used.

an illustration of the box volume used in the heat flux calculations). Using Leibniz's integral rule, we get the following formula for the temperature difference along the WSS:

$$d\overline{T} = \frac{-Q}{\rho c \frac{dV}{dt}}, \qquad (10)$$

determined by the heat loss $Q = 1.4$ TW (1 TW $= 1 \times 10^{12}$ W) to the shelf and the mean volume transport $dV/dt = 1.0$ Sv in the upper 250 m of the barotropic WSC branch. The transport calculation is laterally restricted between the offshore and shelf-side half widths of the jet. The product $\rho c = 4.2$ MJ (K m^3)$^{-1}$. Mean transport was calculated by time integration of the fitted skewed Gaussian profile (Figure 4) for the upper 250 m, and the corresponding mean cross-sectional transport area used in the volume calculations was $A_{slope} = 5.6$ km^2. When estimating the heat loss Q in the northward flowing Atlantic water, we assume the calculated heat flux divergence from period 2 to be valid, which by (10) becomes $d\overline{T} \sim -0.3°$C along the whole 400 km WSS. This corresponds to a heat loss of $-0.08°$C per 100 km that will be compared to earlier estimates.

4.3. Comparison With Earlier Results

[37] *Hanzlick* [1983] disregarded barotropic instability as an active mechanism behind low-frequency waves in the WSC. He based his conclusions upon scaling arguments and results from a basic model derived by *Niiler and Mysak*

[1971]. In their model, the current profile is triangular and the topography is step-like. Hanzlick assumed half widths of more than 20 km, a choice that would lead to the same conclusion with the model used in the present study (see Figure 7b). However, the more detailed current profile inferred from increased mooring coverage clearly shows that the barotropic WSC branch over the upper continental slope is narrower and asymmetrical, which results in a shear that is sufficiently sharp to give rise to instabilities.

[38] Coherent eddies originating from the WSC are commonly observed within the Fram Strait [*Johannessen et al.*, 1983]. Eddies advect sea ice into contact with the Atlantic water masses, causing a rapid retreat of the ice edge (*Johannessen et al.* [1987] reported up to 1–2 km d^{-1}). Several of the eddies were described as originating in the WSC. The present study provides evidence that unstable vorticity waves are frequently generated in the barotropic WSC branch, constituting a potential spawning mechanism for coherent eddies.

[39] On the basis of the fitted current profile, an estimate of the volume transport of the barotropic slope jet can be calculated. The total depth-integrated mean transport for the entire period (October 2007 to June 2008) is 3.6 Sv. This is twice as much as the value for the Svalbard branch reported by *Schauer et al.* [2004] and 20% lower than the 4.6 Sv of annual barotropic transport estimated by *Hanzlick* [1983]. *Schauer et al.* [2004] defined the Svalbard branch as shallower than 1000 m and did not have a current meter east of F1, whereas the present estimate includes the tails of the slope jet, which extend further offshore and further onto the shelf. *Hanzlick* [1983] had fewer current meters and did not distinguish between the slope branch and the offshore branch. Our transport estimate is proportional to the width of the current, whereas unstable conditions are associated with a sharp shear in the current profile. Hence, unstable episodes usually occur when the transport is moderate.

[40] For heat loss estimates by isopycnal diffusion, only the volume flow of the barotropic WSC branch in direct contact with the shelf (the upper 250 m) is used (1.0 Sv). The 1.4 TW heat loss of the northward transported AW due to unstable vorticity waves along the WSS, through an area of $A_{shelf} = 100$ km^2, is found to give a temperature loss of 0.08°C per 100 km. Here we assume that vorticity waves detected in a data set from one slope section are valid for the whole 400 km WSS in an attempt to compare with the observationally based north–south winter temperature gradient of *Saloranta and Haugan* [2004]. Our temperature gradient is only 25% of their 0.31°C per 100 km gradient, and there are obviously along-slope variations and other important processes not accounted for. Westward isopycnal diffusion through vorticity waves [*Nilsen et al.*, 2006] and topographically steered onshore transport of AW are candidates that will be dealt with in subsequent papers. Furthermore, our estimates are based on results from unstable events in the barotropic WSC branch during one winter (2008), while *Saloranta and Haugan* [2004] based their along-slope winter temperature gradient on CTD data from several winters, with stations as far south as 74°N.

[41] Locally across the mooring section, estimated heat loss through vortex dynamics accounted for 50%–60% of the observed temperature drop when the unstable vorticity

waves were present in the data set. We therefore feel confident that isopycnal diffusion generated through barotropic instability is an important process in the heat loss budget along the WSS. Unstable vortices are detected in our mooring section, and their existence is explained through our dynamical stability analysis. In order to estimate the interannual variability of the total heat loss along the WSS, vortex generation mechanisms for the entire slope will be studied.

5. Conclusions

[42] The barotropic WSC branch has been proven to exhibit an asymmetric current profile, giving rise to a sharp shear on the shelf side. The asymmetric profile has been mathematically represented by introducing a skew Gaussian jet profile. The skew Gaussian jet profile was fitted to the smoothed time series of current meter measurements from the upper slope domain and was used as input to a numerical linear stability analysis. The analysis indicated that the barotropic WSC branch experienced several episodes of unstable conditions from December 2007 to May 2008. The characteristic wavelength of the resulting unstable vorticity waves was 20–40 km, with associated wave periods of 40–70 h. A detailed sensitivity analysis showed that the skew profile is most stable when the current maximum is positioned close to F2 (over the steepest part of the slope). When the current maximum moves shoreward (toward F1), it becomes unstable for relatively moderate current speeds. Wavelet analysis detected significant energy at similar periods and time intervals as the stability analysis indicated. In particular, inner and outer rotary spectra of F0 and F1 showed that the 48 h wave period stands out as a robust estimate. Through complex demodulation of the current and temperature data the 48 h signal was studied in detail and two episodes of intense onshore heat flux were identified. During these episodes, the heat loss contribution through isopycnal diffusion was significant and could explain up to 50%–60% of the total observed local heat loss.

References

Aagaard, K., and P. Greisman (1975), Toward new mass and heat budgets for the Arctic Ocean, *J. Geophys. Res.*, 80(27), 3821–3827.
Aagaard, K., A. Foldvik, and S. R. Hillman (1987), The West Spitsbergen Current: Disposition and water mass transformation, *J. Geophys. Res.*, 92(C4), 3778–3784.
Bourke, R. H., A. M. Weigel, and R. G. Paquette (1988), The westward turning branch of the West Spitsbergen Current, *J. Geophys. Res.*, 93(C11), 14,065–14,077.
Boyd, T. J., and E. A. D'Asaro (1994), Cooling of the West Spitsbergen Current: Wintertime observations west of Svalbard, *J. Geophys. Res.*, 99(C11), 22,597–22,618.
Collings, I. L., and R. Grimshaw (1980), The effect of topography on the stability of a barotropic coastal current, *Dyn. Atmos. Oceans*, 10, 83–106.
Collings, I. L., and R. Grimshaw (1984), Stable and unstable barotropic waves in a coastal current, *Geophys. Astrophys. Fluid Dyn.*, 29, 179–220.
Cottier, F., V. Tverberg, M. Inall, H. Svendsen, F. Nilsen, and C. Griffiths (2005), Water mass modification in an Arctic fjord through cross-shelf exchange: The seasonal hydrography of Kongsfjorden, Svalbard, *J. Geophys. Res.*, 110, C12005, doi:10.1029/2004JC002757.
Davies, A. M., J. Xing, and B. Gjevik (2003), Barotropic eddy generation by flow instability at the shelf edge: Sensitivity to open boundary conditions, inflow and diffusion, *J. Geophys. Res.*, 108(C2), 3035, doi:10.1029/2001JC001137.
Davies, K. A., J. J. Leichter, J. L. Hench, and S. G. Monismith (2008), Effects of western boundary current dynamics on the internal wave field of the southeast Florida shelf, *J. Geophys. Res.*, 113, C09010, doi:10.1029/2007JC004699.
Dmitrenko, I. A., I. V. Polyakov, S. A. Kirillov, L. A. Timokhov, I. E. Frolov, V. T. Sokolov, H. L. Simmons, V. V. Ivanov, and D. Walsh (2008), Toward a warmer Arctic Ocean: Spreading of the early 21st century Atlantic Water warm anomaly along the Eurasian Basin margins, *J. Geophys. Res.*, 113, C05023, doi:10.1029/2007JC004158.
Emery, W. J., and R. E. Thomson (Eds.) (2001), *Data Analysis Methods in Physical Oceanography*, 2nd ed., Elsevier, Amsterdam.
Fahrbach, E., G. Rohardt, U. Schauer, J. Meincke, S. Østerhus, and J. Verduin (2003), Direct measurements of heat and mass transports through Fram Strait, *ICES Mar. Sci. Symp.*, 291, 378–381.
Gascard, J.-C., C. Richez, and C. Rouault (1995), New insights on large-scale oceanography in Fram Strait: The West Spitsbergen Current, in *Arctic Oceanography: Marginal Ice Zones and Continental Shelves*, *Coastal Estuarine Stud.*, vol. 49, pp. 131–182, AGU, Washington, D. C.
Gjevik, B. (2002), Unstable and neutrally stable modes in barotropic and baroclinic shelf slope currents, *Preprint Ser. 1*, Dep. of Math., Univ. of Oslo, Oslo.
Hall, R. E. (1980), A note on a semicircle theorem, *Dyn. Atmos. Oceans*, 10, 113–121.
Hanzlick, D. J. (1983), The West Spitsbergen Current: Transport, forcing and variability, Ph.D. thesis, Univ. of Wash., Seattle.
Helland-Hansen, B., and F. Nansen (1912), *The Sea West of Spitsbergen*, *Vidensk. Skr. I Mat. Naturvidensk. Klasse*, vol. 2, 89 pp., Jacob Dybwad, Oslo.
Howard, L. N. (1961), Note on a paper of John W. Miles, *J. Fluid Mech.*, 10, 509–512.
Jakobsson, M., R. Macnab, L. Mayer, R. Anderson, M. Edwards, J. Hatzky, H. W. Schenke, and P. Johnson (2008), An improved bathymetric portrayal of the Arctic Ocean: Implications for ocean modeling and geological, geophysical and oceanographic analyses, *Geophys. Res. Lett.*, 35, L07602, doi:10.1029/2008GL033520.
Johannessen, J. A., et al. (1987), Mesoscale eddies in the Fram Strait marginal ice zone during the 1983 and 1984 Marginal Ice Zone Experiments, *J. Geophys. Res.*, 92(C5), 6754–6772.
Johannessen, O. M., J. A. Johannessen, J. Morison, B. A. Farrelly, and E. A. S. Svendsen (1983), Oceanographic conditions in the marginal ice zone north of Svalbard in early fall 1979 with an emphasis on mesoscale processes, *J. Geophys. Res.*, 88(C5), 2755–2769.
Kasajima, Y., and H. Svendsen (2002), Tidal features in the Fram Strait, *Cont. Shelf Res.*, 22(17), 2461–2477, doi:10.1016/S0278-4343(02)00132-2.
Lilly, J. M., P. B. Rhines, F. Schott, K. Lavender, J. Lazier, U. Send, and E. D'Asaro (2003), Observations of the Labrador Sea eddy field, *Prog. Oceanogr.*, 59(1), 75–176.
Livingstone, D., and T. C. Royer (1980), Eddy propagation determined from rotary spectra, *Deep Sea Res., Part A*, 27, 823–835.
Manley, T. (1995), Branching of Atlantic Water within the Greenland-Spitsbergen Passage: An estimate of recirculation, *J. Geophys. Res.*, 100(C10), 20,627–20,634.
Morison, J. (1991), Seasonal variations in the West Spitsbergen Current estimated from bottom pressure measurements, *J. Geophys. Res.*, 96(C10), 18,381–18,395.
Mysak, L. A. (1980), Recent advances in shelf wave dynamics, *Rev. Geophys.*, 18(1), 211–241.
Niiler, P. P., and L. A. Mysak (1971), Barotropic waves along an eastern continental shelf, *Geophys. Fluid Dyn.*, 2, 273–288.
Nilsen, F., B. Gjevik, and U. Schauer (2006), Cooling of the West Spitsbergen Current: Isopycnal diffusion by topographic vorticity waves, *J. Geophys. Res.*, 111, C08012, doi:10.1029/2005JC002991.
Pedlosky, J. (1987), *Geophysical Fluid Dynamics*, 2nd ed., Springer, New York.
Poulin, F. J., and G. R. Flierl (2005), The influence of topography on the stability of jets, *J. Phys. Oceanogr.*, 35, 811–825.
Press, W. H., S. A. Teukolsky, W. T. Vetterling, and B. P. Flannery (1992), *Numerical Recipes in Fortran 77: The Art of Scientific Computing*, vol. 1, 2nd ed., Cambridge Univ. Press, Cambridge.

Quadfasel, D., J.-C. Gascard, and K.-P. Koltermann (1987), Large-scale oceanography in Fram Strait during the 1984 Marginal Ice Zone Experiment, *J. Geophys. Res.*, *92*(C7), 6719–6728.

Saloranta, T. M., and P. M. Haugan (2001), Interannual variability in the hydrography of Atlantic water northwest of Svalbard, *J. Geophys. Res.*, *106*(C7), 13,931–13,943.

Saloranta, T. M., and P. M. Haugan (2004), Northward cooling and freshening of the warm core of the West Spitsbergen Current, *Polar Res.*, *23*(1), 79–88.

Saloranta, T. M., and H. Svendsen (2001), Across the Arctic front west of Spitsbergen: High-resolution CTD sections from 1998–2000, *Polar Res.*, *20*(2), 177–184.

Schauer, U., E. Fahrbach, S. Østerhus, and G. Rohardt (2004), Arctic warming through the Fram Strait: Oceanic heat transport from 3 years of measurements, *J. Geophys. Res.*, *109*, C06026, doi:10.1029/2003JC001823.

Schauer, U., A. Beszczynska-Möller, W. Walczowski, E. Fahrbach, J. Piechura, and E. Hansen (2008), Variation of measured heat flow through the Fram Strait between 1997 and 2006, in *Arctic-Subarctic Ocean Fluxes*, edited by R. R. Dickson, J. Meincke, and P. Rhines, pp. 65–85, Springer, Dordrecht, Netherlands.

Thiem, O., J. Berntsen, and B. Gjevik (2006), Development of eddies in an idealised shelf slope area due to an along slope barotropic jet, *Cont. Shelf Res.*, *26*(12–13), 1481–1495, doi:10.1016/j.csr.2006.02.016.

Torrence, C., and G. P. Compo (1998), A practical guide to wavelets, *Bull. Am. Meteorol. Soc.*, *79*(1), 61–78.

Tverberg, V., and O. A. Nst (2009), Eddy overturning across a shelf edge front: Kongsfjorden, West Spitsbergen, *J. Geophys. Res.*, *114*, C04024, doi:10.1029/2008JC005106.

Walczowski, W., and J. Piechura (2007), Pathways of the Greenland Sea warming, *Geophys. Res. Lett.*, *34*, L10608, doi:10.1029/2007GL029974.

Walczowski, W., J. Piechura, R. Osinski, and P. Wieczorek (2005), The West Spitsbergen Current volume and heat transport from synoptic observations in summer, *Deep Sea Res., Part I*, *52*, 1374–1391, doi:10.1016/j.dsr.2005.03.009.

B. Gjevik, Department of Mathematics, University of Oslo, PO Box 1053, Blindern, N-0316 Oslo, Norway.

F. Nilsen and S. H. Teigen, Department of Arctic Geophysics, University Centre in Svalbard, PO Box 156, N-9171 Longyearbyen, Norway. (sigurd.henrik.teigen@unis.no)